High redshift FRII radio sources: large-scale X-ray environment

E. Belsole[1,2]⋆, D. M. Worrall[2], M.J. Hardcastle[3], & J. H. Croston[3]

[1] *Institute of Astronomy, University of Cambridge, Madingley Road, Cambridge, CB3 0HA, U.K.*
[2] *Department of Physics, University of Bristol, Tyndall Avenue, Bristol BS8 1TL, U.K.*
[3] *School of Physics, Astronomy and Mathematics, University of Hertfordshire, College Lane, Hatfield, Hertfordshire AL10 9AB, U.K.*

ABSTRACT

We investigate the properties of the environment around 20 powerful radio galaxies and quasars at redshifts between 0.45 and 1. Using *XMM-Newton* and *Chandra* observations we probe the spatial distribution and the temperature of the cluster gas. We find that more than 60 per cent of powerful radio sources in the redshift range of our sample lie in a cluster of X-ray luminosity greater than 10^{44} erg s^{-1}, and all but one of the narrow-line radio galaxies, for which the emission from the nucleus is obscured by a torus, lie in a cluster environment. For broad-line quasars the X-ray emission from the core dominates and it is more difficult to measure the cluster environment. However, within the statistical uncertainties we find no significant difference in the properties of the environment as a function of the orientation to the line of sight of the radio jet. This is in agreement with unification schemes. Our results have important implications for cluster surveys, as clusters around powerful radio sources tend to be excluded from X-ray and Sunyaev-Zeldovich surveys of galaxy clusters, and thus can introduce an important bias in the cluster luminosity function. Most of the radio sources are found close to pressure balance with the environment in which they lie, but the two low-excitation radio galaxies of the sample are observed to be under-pressured. This may be the first observational indication for the presence of non-radiative particles in the lobes of some powerful radio galaxies. We find that the clusters around radio sources in the redshift range of our sample have a steeper entropy-temperature relation than local clusters, and the slope is in agreement with the predictions of self-similar gravitational heating models for cluster gas infall. This suggests that selection by AGN finds systems less affected by AGN feedback than the local average. We speculate that this is because the AGN in our sample are sufficiently luminous and rare that their AGN activity is too recent to have caused the onset of measurable feedback and increased entropy in the clusters, especially in the cooler ones where locally the effect of feedback are expected to be most evident. If this is confirmed by forthcoming X-ray missions it will improve our understanding of the heating and cooling processes in high-redshift galaxy clusters.

Key words: galaxies: active – galaxies: high redshift – quasars: general – radio continuum: galaxies – X-rays: galaxies: clusters

1 INTRODUCTION

Much evidence supports the existence of a gaseous environment around powerful radio galaxies and quasars. Theoretically, models of jet confinement imply that an external medium with pressure similar to the pressure found at the centre of galaxy clusters is required to keep the jet collimated (Begelman, Blandford, & Rees 1984). Observationally, two of the most powerful radio galaxies, Cygnus A (Arnaud et al. 1984; Reynolds & Fabian 1996) and 3C 295 (e.g. Henry & Henriksen 1986; Allen et al. 2001), are located in the centre of rich clusters of galaxies. Studies based on optical observations find that, at redshift $\sim 0.2 - 0.3$, power-

ful Fanaroff-Riley type II (FRII) sources are found in relatively modest environments (group scale, e.g., Hill & Lilly 1991; Zirbel 1997; Wold et al. 2000; Best 2004, and references therein), while at higher redshifts the environments of FRIIs may again be rich clusters with richness comparable to Abell class I or higher (e.g., Hall & Green 1998). This evidence is provided mainly by studies based on galaxy over-densities, gravitational arcs (Deltorn et al. 1997; Wold et al. 2002) and lensing shear of surrounding field galaxies (Bower & Smail 1997). Hence it has been apparent for many years that powerful radio galaxies and quasars should act as sign-posts of massive galaxy clusters at high redshift.

The clearest observational evidence for the existence of a cluster around a radio source is the detection of an X-ray emitting, thermal, large-scale medium surrounding it. Using *ROSAT*

⋆ E-mail: elena@ast.cam.ac.uk

Table 1. The sample

Source	RA(J2000) ($^{\mathrm{h\ m\ s}}$)	Dec(J2000) ($^{\circ\ \prime\ \prime\prime}$)	redshift	scale (kpc/arcsec)	type	N_{H} ($\times 10^{20}$ cm $^{-2}$)	Literature
3C 6.1	00 16 30.99	+79 16 50.88	0.840	7.63	NLRG	14.80	this work
3C 184	07 39 24.31	+70 23 10.74	0.994	8.00	NLRG	3.45	B04
3C 200	08 27 25.44	+29 18 46.51	0.458	5.82	LERG	3.74	this work
3C 207	08 40 47.58	+13 12 23.37	0.684	7.08	LDQ	4.12	Br02/G03
3C 220.1	09 32 39.65	+79 06 31.53	0.610	6.73	NLRG	1.87	W01
3C 228	09 50 10.70	+14 20 00.07	0.552	6.42	NLRG	3.18	this work
3C 254	11 14 38.71	+40 37 20.29	0.734	7.28	LDQ	1.90	CF03/D03
3C 263	11 39 57.03	+65 47 49.47	0.646	6.90	LDQ	1.18	CF03/H02
3C 265	11 45 28.99	+31 33 49.43	0.811	7.54	NLRG	1.90	this work
3C 275.1	12 43 57.67	+16 22 53.22	0.557	6.40	LDQ	1.99	CF03
3C 280	12 56 57.85	+47 20 20.30	0.996	8.00	NLRG	1.13	D03
3C 292	13 50 41.95	+64 29 35.40	0.713	6.90	NLRG	2.17	B04
3C 295	14 11 20.65	+52 12 09.04	0.461	5.530	NLRG	1.32	A01
3C 309.1	14 59 07.60	+71 40 19.89	0.904	7.80	GPS-Q	2.30	this work
3C 330	16 09 34.71	+65 56 37.40	0.549	6.41	NLRG	2.81	H02
3C 334	16 20 21.85	+17 36 23.12	0.555	6.38	LDQ	4.24	this work
3C 345	16 42 58.80	+39 48 36.85	0.594	6.66	CDQ	1.13	G03
3C 380	18 29 31.78	+48 44 46.45	0.691	7.11	CDQ	5.67	this work
3C 427.1	21 04 06.38	+76 33 11.59	0.572	6.49	LERG	10.90	this work
3C 454.3	22 53 57.76	+16 08 53.72	0.859	7.68	CDQ	6.50	this work

Galactic column density is from Dickey & Lockman (1990); NLRG means Narrow Line Radio Galaxy; LERG means low-excitation radio galaxy, this is defined following Jackson & Rawlings (1997) as having [O III]/H$_\alpha$ < 0.2 and equivalent widths of [O III]< 3 Å; LDQ means lobe-dominated quasar and CDQ means core-dominated quasar. The two classes of quasars are defined such that the ratio R of core to extended (lobe) flux density at 5 GHz (wherever available) on arc second scales is $R > 1$ for CDQ (e.g. Ghisellini et al. 1993). GPS indicates Gigahertz Peaked Spectrum sources. Redshifts and positions are taken from Laing, Riley & Longair (1983). References in the last column are to papers searching for extended emission using data from the same observatory as used here: A01: Allen et al. 2001; B04: Belsole et al. 2004; Br02: Brunetti et al. 2002; CF03: Crawford & Fabian 2003; D03: Donahue et al. 2003; G03: Gambill et al. 2003 (this work does not find any cluster-like environment around the sources overlapping with our sample); H02: Hardcastle et al. 2002; W01: Worrall et al. 2001.

data, a number of objects at > 0.5 were inferred to lie in moderate to rich clusters (e.g., Worrall et al. 1994; Crawford et al. 1999; Hardcastle & Worrall 1999, 2000). However, the limited sensitivity and resolution of the instruments on-board *ROSAT* did not allow spectral confirmation of these results, and in some cases emission from the central AGN was not separated from the extended component.

X-ray studies of the cluster-like environment of radio sources are complicated by the X-ray emission of other components, particularly the AGN nucleus and radio lobes. The greatly improved spatial resolution of the *Chandra* observatory confirmed some of the clusters detected with *ROSAT* (Worrall et al. 2001; Hardcastle et al. 2002) and found new clusters (e.g. Siemiginowska et al. 2005). A few observations with *XMM-Newton* added to the cluster detections around radio sources (Belsole et al. 2004). However, studies based on small samples claim that inverse Compton (IC) emission coincident with the radio lobes dominates the X-ray extended emission associated with at least some FRIIs at high redshift (e.g., Donahue et al. 2003; Carilli et al. 2002; Hardcastle et al. 2002), obscuring most of the measurable thermal, cluster-like emission (e.g., Fabian et al. 2003). These studies thus need a precise modelling of the Point-Spread-Function (PSF) and a precise measurement of the non-thermal diffuse IC emission often found to coincide with the radio lobes. What has been lacking until now is a uniform analysis of a reasonably sized sample of objects aimed at characterising the cluster X-ray emission, separating it from the emission from the nucleus and radio lobes.

The cluster luminosity function can be used to place stringent constraints on cosmological models (e.g., Evrard 1989; Oukbir & Blanchard 1992; Eke et al. 1998; Schuecker et al. 2003), and the detection of a large number of clusters, in X-ray or via the Sunyaev-Zeldovich (SZ) effect, is more efficient than measuring the redshift of millions of galaxies, especially at high redshifts (e.g., Schuecker et al. 2001). Although some high-redshift ($z > 1$) galaxy clusters have been detected lately as serendipitous sources (e.g. Mullis et al. 2005; Stanford et al. 2006, and references therein), measurements of the typical gas mass and luminosity of clusters around active galaxies is lacking. This has important implications because in the local universe 70 per cent or more of massive clusters appear to harbour an active galaxy at their centre, and at earlier times it is expected that galaxies are more active, so that failing to include these objects in the cluster luminosity function may result in an important bias (Willott et al. 2001; Celotti & Fabian 2004; Belsole, Fabian, Erlund, in preparation). This bias may be a function of cosmic time since there are suggestions that the richness of radio-galaxy environments evolves with time, so that the detection and investigation of active galaxy environments will allow us to map the cosmic evolution of structure, which would be hampered by a pure X-ray or optical selection.

The study of the X-ray cluster environments around radio sources is important in itself for furthering our understanding of accretion mechanisms and AGN feedback, particularly in comparison with local sources. At low redshift FRIIs and less powerful FRI radio galaxies seem to lie in different environments, with the latter preferring richer media (Hardcastle & Worrall 1999); the study of radio galaxies at different redshifts therefore allows us to shed light

on the effect of the environment on the radio galaxy properties and the accretion mechanisms at various look-back times. Furthermore, a comparison between environments of radio sources with jets at different angles to the line of sight is a powerful way of testing orientation-based unification models.

In this paper we present the first systematic X-ray study of the extended emission from powerful radio galaxies at $z > 0.45$ to have been carried out with the current generation of X-ray satellites, using a moderately large sample of 20 radio galaxies and quasars from the same catalogue. Of the 20 sources, 11 have previously published studies of their extended X-ray emission; 5 of these were studied by our group. Table 1 gives references to the literature for these objects. Clusters around 5 more sources are detected in this paper for the first time. The X-ray properties of the nuclei of this sample were discussed in Belsole, Worrall, Hardcastle (2006). The lobe IC emission from most of the sources was described in Croston et al. (2005b). In this paper we report the properties of the external environments around the sources in our sample.

Throughout the paper we use a cosmology with $H_0 = 70$ km s^{-1} Mpc^{-1}, $\Omega_m = 0.3$, $\Omega_\Lambda = 0.7$. If not otherwise stated, errors are quoted at the 1σ confidence level.

2 THE SAMPLE

This study is based on the sample described in Belsole et al. (2006). Sources are taken from the 3CRR catalogue (Laing et al. 1983), which is selected on the basis of low-frequency (178-MHz) radio emission, and are in the redshift range $0.45 < z < 1.0$. In the present paper we have added one source, 3C 295, to the original sample. 3C 295 was not investigated by Belsole et al. (2006) as it was not part of the *Spitzer* sample discussed in the above paper, although its nuclear X-ray properties were discussed by Hardcastle, Evans & Croston (2006). For consistency reasons we include it in the present sample. 3C 295 is a complex source in the X-ray and the detailed analysis of its properties is not comparable with the more global analysis that can be carried out with the other sources in our sample, which is limited by photon statistics. As a result, a detailed re-analysis of the source similar to the one carried out by Allen et al. (2001) is beyond the scope of this paper. For the present work we limit ourselves to derive global properties from the 90 ks ACIS-I observation of 3C 295, which, with an exposure 5 times longer, offers a much better statistics than the early ACIS-S observation used by Allen et al. This approach makes us confident that we are comparing this extreme source to the other sources in the sample by treating it in a similar way.

The sample is composed of a similar number of broad-line quasars and narrow-line radio galaxies. Table 1 lists the main properties of the sources including their quasar classification.

Preparation of the *Chandra* data is described in Belsole et al. (2006). However for this paper we re-processed the data with CIAO 3.3.0.1 and CALDB v3.2.4, and added observation ID 4843 of 3C 454.3 and ID 2254 of 3C 295. *XMM-Newton* data preparation is described in Belsole et al. (2004), and we use the same data and results for this analysis. In Table 2 we give details of the X-ray observations used in this work.

3 SPATIAL ANALYSIS

3.1 Imaging

Diffuse, thermal X-ray emission associated with a cluster-like environment is best detected at soft energies, between 0.5 and 2.5 keV, as this is the energy range where the *Chandra* and *XMM-Newton* mirrors are the most sensitive. Thermal bremsstrahlung cluster radiation peaks in this energy range, while the nuclear X-ray component and the lobe inverse-Compton emission tends to have a harder spectrum. For this reason we generated images of each source in the 0.5-2.0 keV (soft) and 2.5-7.0 keV (hard) energy bands (we adopt a separation of 500 eV in order to avoid features associated with the Si edges, and also to ensure that the two energy bands do not overlap). We then applied a wavelet reconstruction algorithm provided by A. Vikhlinin[1] as an efficient way to search for extended emission not associated with the PSF, and at a detection limit of 4.5σ above the background level at the location of each pixel. In Appendix A we show for each source observed with *Chandra* the wavelet-decomposed and reconstructed images in the soft and hard band. The same analysis for 3C 184 and 3C 292 was presented by Belsole et al. (2004) and so is not repeated here. The radio emission at 1.4 GHz is shown by the superimposed logarithmic contour. The comparison between the images at soft and hard energy bands gives an immediate indication of the presence of extended X-ray emission which may be associated with an external environment of the radio source. For most of the sources, extended X-ray emission seems to be associated with the radio lobes, but many of the sources also show more symmetrical emission which tends to fade at high energy.

3.2 Radial profile

We carried out a more quantitative characterisation of the spatially extended emission by extracting a radial profile of each source. The profile was centred on the emission peak of each source, and point sources other than the central AGN were excluded. Here we focus on extended emission associated with the external environment and not the extended non-thermal X-ray emission associated with the lobes (Croston et al. 2005b). Although in Croston et al. we showed that many of the sources in the sample contribute very few counts to the lobe emission, to be conservative we excluded the spatial regions coincident with the radio lobes before extracting the radial profile. The masked area was properly taken into account when deriving physical parameters. Any emission at radio frequencies from the CDQs – not discussed in Croston et al. (2005b) – is within 5 arcsec of the centre of the source and so not relevant to the analysis discussed here. For details of the detection of X-ray counterparts of three of the sources see Sambruna et al. (2002) (3C 345), Marshall et al. (2005) (3C 380), and Marshall et al. (2005); Tavecchio et al. (2007) (3C 454.3).

We used the energy band 0.5-2.5 keV which optimises the instrument sensitivity to the soft thermal emission over the AGN and particle contributions. Exposure corrections were applied using a map calculated at the peak energy of the global spectrum, which was found to be at 1 keV for most of the sources. When multiple exposures were available, the radial profile was extracted from a mosaic event list and the mosaic exposure map was used. The background region was chosen by selecting an annular region between the distance from the centre at which the radial profile becomes flat

---

[1] http://hea-www.harvard.edu/RD/zhtools/

Table 2. Observation log. Col 1: 3CRR name; Col. 2: Instrument used for the observations, C stands for *Chandra*, X for *XMM-Newton*; Col.3: Observation ID; Col. 4: Nominal exposure Time; Col. 5: Net exposure time, after flare screening. For *XMM-Newton* observations we give times for mos/pn detectors; Col. 6 pileup fraction.

Source	Instrument	Obs ID	EXPOSURE (ks)	Screened time (ks)	pileup
3C 6.1	C	4363	20	20.0	5
	C	3009	36	35.7	5
3C 184	C	3226	20	18.9	1
	X	0028540201	38.9	32/–	na
	X	0028540601	40.9	26/16.4	na
3C 200	C	838	16	14.7	1
3C 207	C	2130	39	37.5	22
3C 220.1	C	839	21	18.5	7
3C 228	C	2453	12	10.6	2
	C	2095	15.5	13.8	3
3C 254	C	2209	31	29.5	20
3C 263	C	2126	51	48.8	26
3C 265	C	2984	59	50.6	1
3C 275.1	C	2096	26	24.8	4
3C 280	C	2210	63.5	46.3	< 1
3C 292	X	0147540101	33.9	20/17	< 1
3C 295	X	2254	92.1	90.9	0
3C 309.1	C	3105	17	16.6	6
3C 330	C	2127	44	43.8	0
3C 334	C	2097	33	30.2	9
3C 345	C	2143	10	9.0	13
3C 380	C	3124	5.5	5.3	16
3C 427.1	C	2194	39	39.0	0
3C 454.3	C	3127	5.5	5.5	24
	C	4843	18.3	18.0	17

and at which it increases because particle-dominated background has been erroneously corrected for vignetting. The inner radius of the background annulus is specific to each source (see Table 3). We limited our analysis to the S3 chip in all cases but 3C 295 (ACIS-I), and the background area was also selected from this chip.

To assert the presence of extended emission, modelling of the PSF is crucial, especially in the context of these sources which harbour bright AGN. To obtain the best representation of the central point source emission we generated a model of the PSF at the off-axis position of each source using the Chandra Ray Tracer (ChaRT) and MARX[2]. We used the option of giving the spectrum of the source as the input parameter in order to generate a PSF model appropriate for the spectral distribution. The output file of ChaRT was then used to generate an event list of the PSF using MARX. We then extracted a radial profile of the PSF for each source and used this model to fit the source radial profile. We adopted an iterative process as the PSF model is dependent on the blurring parameter which is an input to MARX. We changed this parameter in order for the PSF to fit the first two bins of the radial profile of the source. For sources with a pileup fraction of more than 10 per cent we used MARX to generate a piled-up PSF model and we used this event list as the best representation of the point source. Radial profiles were initially fitted with a PSF. When this was not an acceptable fit, we added a β-model. We varied the β parameter and core-radius, r_c, when the photon statistics were sufficient to carry out a two-parameter fit. In all other cases we fixed the β and r_c parameters to values (generally 2/3, and 120-150 kpc) commonly observed in local clusters, allowing for the possibility that clusters at high redshift are more concentrated (i.e. smaller core radii and
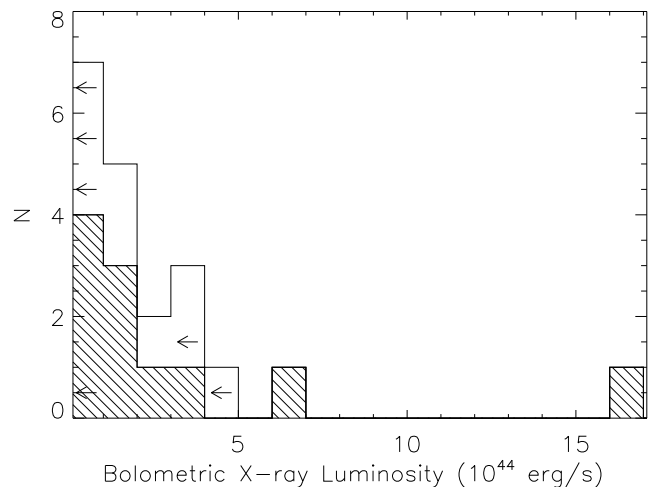

Figure 1. Bolometric X-ray luminosity distribution. The shaded area corresponds to the radio galaxies sub-sample

β than canonical values in the local universe should not be seen as unusual). The results of the radial profile fitting are listed in Table 3, and the individual fits can be inspected in Appendix A for the sources observed with *Chandra*, while for 3C 184 and 3C 292, observed with *XMM-Newton*, the profiles are shown in Belsole et al. (2004).

4 SPECTRAL ANALYSIS

We selected the spatial region for spectral extraction on the basis of the shape of the radial profile. We initially extracted a background-
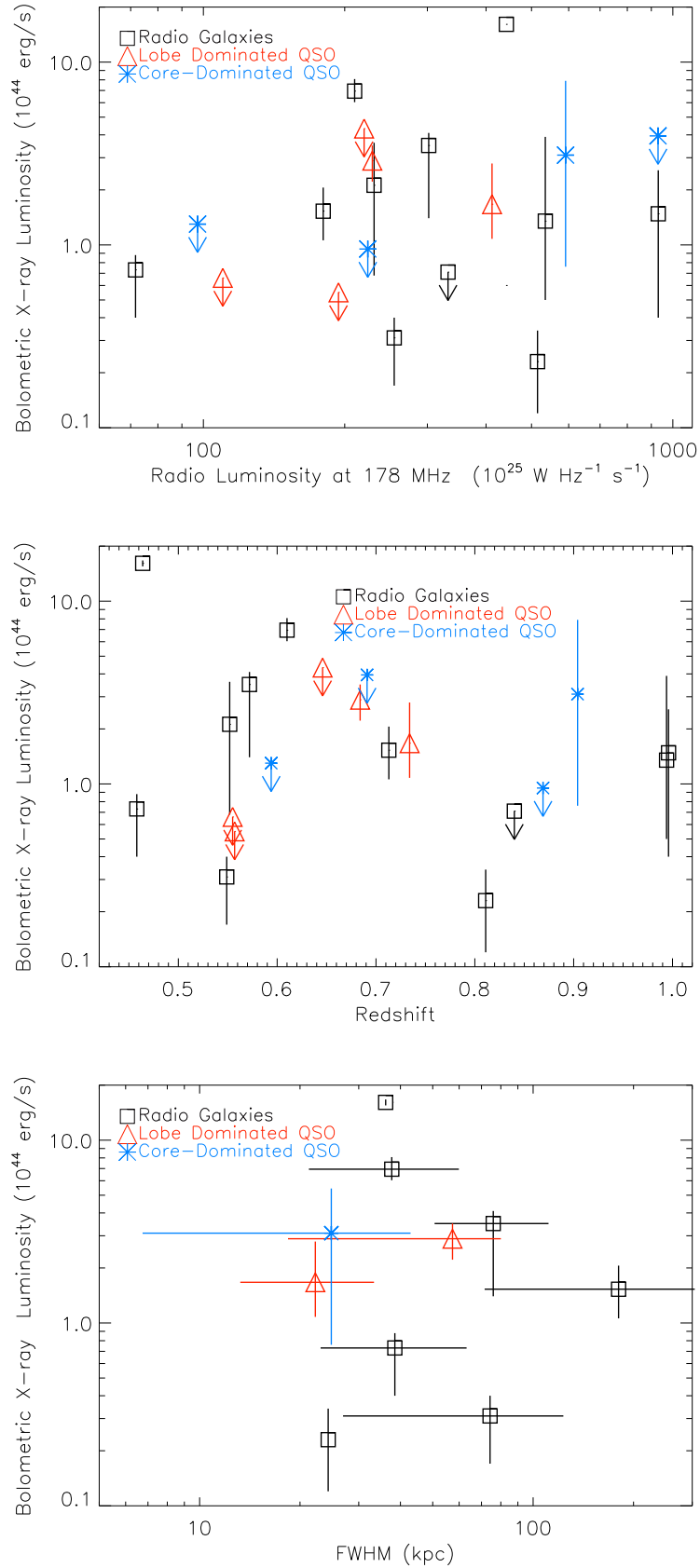
Figure 2. Top: Bolometric X-ray luminosity versus radio power of each galaxy as measured at 178 MHz. Middle: Bolometric X-ray luminosity versus redshift. Bottom: Bolometric X-ray luminosity versus Full-Width-Half-Maximum (r_{FWHM}) defined as in Eq. 2. Only sources for which fitting of β and r_c were possible are used for this plot.

Table 3. Radial profile modelling results. Col. 1: source 3CRR name; Col. 2: quality flag, where C implies a detection of extended emission with constrained structural parameters, D implies a detection with F-test probability for having an extended component > 98 per cent but unconstrained structural parameters, and P implies a point-like source with no detected extended emission; Col. 3: best-fitting beta parameter; Col. 4: best-fitting core radius; Col. 5: number of counts predicted by the best fitting β-model included in a circle of radius corresponding to the detection radius $R_{det.}$; Col. 6: external radius of the last annulus used to integrate the profile, this is also the radius of the inner circle of the annulus used for background subtraction; Col. 7: number of counts predicted by the best fitting β-model out to a distance from the centre corresponding to R_{200}; Col. 8: distance from the centre corresponding to the radius at which the density of the cluster is equal to an over-density of 200; Col. 9: Central surface brightness of the β-model; Col. 10: χ^2/d.o.f. corresponding to the best-fitting β-model+PSF. If "UL" a 3σ upper limit was calculated using appropriate values of β and r_c; Col. 11: χ^2/d.o.f. corresponding to the best-fitting PSF model only; Col. 12: F-test null probability that the two-component model gives an improved fit for random data.

Source	qual	beta	r_c (arcsec)	$cnt_{det.}$	$R_{det.}$ (arcsec)	$cnt(R_{200})$	R_{200} (kpc)	S_0 (cts arcsec^{-2})	χ^2/d.o.f.	χ^2 (PSF fit)	F-test prob. (per cent)
3C 6.1	P	0.5f	15.0f	< 226	49.2	< 235	620	< 0.01	UL	5.68/8	N/A
3C 184*	D	0.66f	20.0f	63 ± 60	87.5	67^{+118}_{-25}	790	0.03 ± 0.02	0.6/5	3.13/6	5.90e-3
3C 200	C	$1.00^{+0.20}_{-0.40}$	$5.85^{+4.99}_{-3.49}$	160 ± 47	64.0	168 ± 50	1140	2.31 ± 0.69	2.20/3	13.57/6	0.105
3C 207**	D	$0.80^{+0.20}_{-0.30}$	$6.1^{+3.9}_{-4.8}$	342 ± 43	19.8	506^{+958}_{-103}	1146	3.46 ± 0.43	4.61/6	67.60/9	6.76e-4
3C 220.1	C	$0.58^{+0.14}_{-0.08}$	$3.24^{+2.94}_{-1.66}$	852 ± 80	39.4	1021 ± 96	1150	8.80 ± 0.82	6.90/7	121.30/11	1.89e-4
3C 228	D	0.5f	15.0f	122 ± 38	78.7	214 ± 140	1072	0.05 ± 0.01	5.81/7	16.37/8	9.13e-3
3C 254	C	$0.65^{+0.15}_{-0.10}$	$1.95^{+1.50}_{-0.95}$	252 ± 35	39.4	273^{+25}_{-14}	568	10.7 ± 1.5	10.64/7	62.50/10	4.41e-3
3C 263	P	0.67f	10f	< 904	64.0	< 968	1173	< 1.66	UL	86.50/12	N/A
3C 265	D	$1.00^{+1.00}_{-0.33}$	$2.85^{+3.15}_{-1.85}$	53 ± 17	24.6	56 ± 18	436	3.3 ± 1.00	2.54/2	12.03/5	0.299
3C 275.1	P	0.60f	7.0f	< 113	19.7	< 129	494	< 0.34	UL	7.54/7	N/A
3C 280	D	0.50f	8.0f	98 ± 31	32.0	213^{+300}_{-153}	119	0.15 ± 0.05	2.58/4	12.86/5	1.62e-2
3C 292*	C	$0.80^{+0.50}_{-0.25}$	$19.7^{+26.8}_{-14.0}$	523 ± 66	100.0	528^{+111}_{-68}	707	0.40 ± 0.05	1.62/7	65.08/10	5.61e-6
3C 295	C	$0.52^{+0.01}_{-0.01}$	$3.4^{+0.25}_{-0.25}$	11400 ± 75	108.2	13130 ± 160	1268	$55.8^{+2.9}_{-3.4}$	84/55	$3.9 \times 10^5/58$	0
3C 309.1	C	$0.56^{+0.19}_{-0.04}$	$1.78^{+4.24}_{-1.33}$	141 ± 26	39.4	164^{+122}_{-42}	366	3.76 ± 0.68	0.87/3	29.40/6	8.57e-3
3C 330	C	$0.65^{+0.55}_{-0.15}$	$7.40^{+12.1}_{-5.30}$	158 ± 26	39.4	166^{+46}_{-37}	644	0.48 ± 0.08	1.14/3	37.35/6	8.97e-3
3C 334	P	0.67f	10.0f	< 155	35.4	< 191	496	< 0.35	UL	3.54/8	N/A
3C 345	P	0.67f	15.0f	< 127	39.4	< 154	717	< 0.13	UL	6.93/11	N/A
3C 380	P	0.50f	7.0f	< 105	88.6	< 109	677	< 0.13	UL	15.98/9	N/A
3C 427.1	C	$0.50^{+0.05}_{-0.10}$	$5.85^{+3.60}_{-2.85}$	305 ± 37	49.2	894^{+26}_{-444}	1315	0.59 ± 0.07	1.81/4	69.58/7	1.26e-3
3C 454.3	P	0.50f	5.0f	< 385	29.5	< 480	413	< 1.27	UL	14.47/9	N/A

(*) from XMM analysis. The listed values refer to the PN camera only. See Belsole et al. (2004) for details.

(**) although the β-model parameters are constrained we were not able to constrain the temperature of the extended emission. We thus decided to be conservative and give a quality flag D instead of C for this source (see discussion in the text).

subtracted spectrum of the source in the same area as used for the radial profile analysis, but we excluded the nuclear region with circles of radii 2-4 arcsec for the non-piled up sources (weak core or pileup fraction < 10) and up to 10 arcsec when pileup was significant (strong cores, pileup fraction > 10). We also masked the areas coincident with the radio lobes as detailed in the previous section. For those sources with no X-ray lobe detections or upper limits on the X-ray emission from the lobes (Croston et al. 2005b), we did not mask the radio lobe area. In the case of CDQs the radio emission is within the area used to mask the core.

We initially fitted all spectra with a MEKAL model with fixed chemical abundance (using the solar abundances of Grevesse & Sauval 1998). For a number of sources it was necessary to add a power-law model to account for residuals of the PSF. In these cases, to account for the flattening of the power-law spectrum in the wings of the PSF the power-law index was fixed to be at the lower limit of the best-fit spectral index obtained for the core spectrum of the source (Belsole et al. 2006) and we adjusted the normalization of the power-law model to be appropriate for the PSF fraction in the area used for the cluster spectrum. For those sources with no-detected extended thermal emission we calculated 3σ upper limits for a thermal component in addition to the power law. The temperature in this case was fixed between 1 and 5 keV depending on the shape of the power law spectrum.

Results of the spectral analysis are summarised in Table 4.

5   HOW LUMINOUS ARE RADIO GALAXY CLUSTERS ?

The bolometric X-ray luminosity was calculated for each source adopting the spectral best-fit temperature (the fixed value was used when upper limits are considered) and extrapolating the spectrum to the whole energy range, and the β-model out to the virial radius, here assumed to be R_{200}. This was calculated as:

$$R_{200} = h(z)^{-1} \times B_{200} \times (kT/5 \text{ keV})^{\beta} \qquad (1)$$

In the expression above, B_{200} and β are taken from the $R - T$ relation of Arnaud, Pointecouteau & Pratt (2005), using the best-fit or adopted temperature of the cluster from Table 4, and $h^2(z) = \Omega_m(1 + z)^3 + \Omega_\Lambda$.

Uncertainties on the bolometric L_X were computed by adding in quadrature the statistical fractional error on the normalisation of the spectrum and the relative fractional error on the number of counts predicted by the radial-profile best-fit model. Figure 1 shows the distribution of the bolometric X-ray luminosity for the whole sample; the radio galaxy subsample is shown by the shaded area. Upper limits are also included in the histogram.

More than 60 per cent of the radio sources in the sample are found to lie in environments of X-ray luminosity greater than 10^{44} erg s^{-1}, and more than 30 per cent lie in clusters of luminosity greater than 2×10^{44} erg s^{-1}. For 6 out of 9 quasars we were unable to measure the L_X and only an upper limit indicates the brightness of the cluster. On the other hand, only one RG, 3C 6.1, does not show detectable extended emission. We believe that this effect is

Table 4. Spectral analysis: Col. 1: source 3CRR name; Col. 2: radius of the circle used to integrate the spectrum. This may be smaller than the outer circle used to extract the radial profile; Col. 3: number of net counts in the energy range 0.5-2.5 keV contained in the area used for the spectral analysis. This is lower than the number of counts in the radial profile as the area masked before extracting the profile is larger to account for the point source emission. When two values are listed it means that two exposures have been used. For 3C 184 and 3C 292 we list the counts from the whole EPIC; Col. 4: best-fit mekal model temperature and 1 σ errors for one interesting parameter; Col. 5: chemical abundances used for the fit. The Grevesse & Sauval (1998) table for solar abundances was adopted and all values were fixed; Col. 6: Normalisation of the MEKAL model; Col. 7: χ^2/d.o.f. corresponding to the best-fitting model; Col. 8: unabsorbed X-ray flux in the energy range 0.5-2.5 keV; Col. 9: unabsorbed X-ray luminosity of the thermal component in the energy range 0.5-2.5 keV; Col. 10: total (bolometric) X-ray luminosity of the thermal component within the detection radius of the spectrum; Col. 11: Bolometric X-ray luminosity. This was calculated by extrapolating the number of counts out to the virial radius using the radial profile distribution and using the count rate to adjust the normalisation of the spectral model to obtain the bolometric X-ray luminosity. Errors are the quadratic sum of the statistical errors derived from the spectral and radial profile analyses.

Source	R (arcsec)	cnts 0.5-2.5 keV	kT (keV)	$Z/Z_\odot$	Norm ($\times 10^9$ cm^{-5})	χ^2/dof	f_X ($\times 10^{-14}$ erg s^{-1} cm^{-2}) 0.5-2.5 keV	L_X ($\times 10^{43}$ erg s^{-1}) 0.5-2.5 keV	$L_X^{Bol\,sp}$ ($\times 10^{44}$ erg s^{-1})	L_X^{Bol} ($\times 10^{44}$ erg s^{-1}) Extrapol.
3C6.1	49.2	60+14	2.0f	0.5	< 3.24	UL	< 0.72	< 2.1	< 0.59	< 0.71
3C184[a]	40.0	201[b]	$3.6^{+10.7}_{-1.9}$	0.3	$2.27^{+0.53}_{-0.46}$	43.13/47	$0.5^{+0.12}_{-0.10}$	2.1	0.5	$1.35^{+2.55}_{-0.90}$
3C200	24.6	79	$3.91^{+7.67}_{-1.82}$	0.3	$3.40^{+0.63}_{-0.69}$	7.27/10[C]	$1.26^{+0.24}_{-0.52}$	0.1	0.26	$0.73^{+0.15}_{-0.33}$
3C207	19.8	127*	5.0f	0.5	$2.29^{+0.47}_{-0.47}$	5.33/5	$0.8^{+0.2}_{-0.2}$	1.4	0.38	$2.89^{+0.61}_{-0.67}$
3C220.1	24.6	338	$4.65^{+1.29}_{-0.89}$	0.3	$16.38^{+1.18}_{-1.12}$	10.86/13	$5.2^{+0.39}_{-0.34}$	6.9	1.86	$6.94^{+1.14}_{-0.90}$
3C228	49.2	66+66	$3.87^{+6.86}_{-1.51}$	0.3	$7.05^{+1.09}_{-1.02}$	4.86/12	$2.3^{+0.36}_{-0.40}$	2.5	0.62	$2.12^{+1.50}_{-1.44}$
3C254	34.4	82*	$1.54^{+7.06}_{-0.87}$	0.5	$1.33^{+0.87}_{-0.43}$	1.62/3	$0.34^{+0.22}_{-0.11}$	0.9	0.18	$1.67^{+1.12}_{-0.59}$
3C263	64.0	162[b]	5.0f	0.3	< 2.9	UL	< 0.9	1.4	0.38	< 4.33
3C265	24.6	16	$1.05^{+0.34}_{-0.46}$	0.5	$0.55^{+0.23}_{-0.25}$	4.73/5[C]	$0.14^{+0.06}_{-0.06}$	0.6	0.10	$0.23^{+0.11}_{-0.11}$
3C275.1	19.7	8	1.0f	0.3	< 0.86	UL	< 0.35	0.5	0.09	< 0.55
3C280	20.0	53	5.0f	0.3	$1.52^{+0.34}_{-0.39}$	0.41/3[C]	$0.34^{+0.07}_{-0.09}$	1.3	0.40	$1.48^{+1.08}_{-1.08}$
3C292[a]	100	310	$2.18^{+3.12}_{-0.83}$·	0.3	$5.85^{+1.57}_{-1.62}$	10.58/12	$1.47^{+0.41}_{-0.41}$	3.11	0.64	$1.53^{+0.53}_{-0.47}$
3C 295	108.2	8034	$4.74^{+0.26}_{-0.23}$	0.48±0.08	133±5	163/190	52±2	36	9.86	16.1 ± 0.6
3C309.1	32.0	31*	$0.87^{+0.86}_{-0.07}$	0.7	$1.11^{+1.52}_{-0.79}$	0.34/4[C]	$0.24^{+0.33}_{-0.17}$	1.74	0.29	$3.1^{+4.80}_{-2.34}$
3C330	39.4	146	$1.59^{+3.78}_{-0.63}$	0.2	$2.57^{+0.30}_{-0.97}$	1.48/6[C]	$0.63^{+0.07}_{-0.24}$	0.82	0.17	$0.31^{+0.09}_{-0.14}$
3C334	35.4	24	1.0f	0.5	< 2.51	UL	< 1.04	0.15	0.25	< 0.66
3C345	39.4	37*	2.0f	0.5	< 4.43	UL	< 1.15	0.20	0.40	< 1.3
3C380	88.6	76*	2.0f	0.5	< 11.7	UL	< 3.11	6.8	1.36	< 3.95
3C427.1	24.6	168	$5.66^{+9.59}_{-2.35}$	0.3	$3.39^{+0.60}_{-0.57}$	3.94/3	$1.2^{+0.20}_{-0.20}$	1.27	0.38	$3.5^{+0.60}_{-2.10}$
3C454.3	29.5	77+31*	1.0f	0.5	< 4.2	UL	< 1.0	5.5	0.96	< 0.95

* counts are partially from the wings of the PSF and have been modelled before extracting the thermal model values.

[a] See Belsole et al. (2004) for details. For 3C 184 the number of counts and the χ^2 correspond to the whole spectral region (nucleus not excluded) and fitted model. For 3C 292, the area used for the spectral analysis was an ellipse on major and minor semi-axis equal to 101 and 64 arcsec respectively. A sector in the region corresponding to the radio lobes was also excluded.

[b] 3C263: All counts are from a point source; 3C 184: part of the counts are from the point source as it cannot be resolved with XMM data

[C] C-statistics were used, and the values quoted are the C-statistic parameter and the Pulse Height Amplitude (PHA).

mostly due to observational constraints: the quasars of the sample have bright cores and they have been targeted mainly to study the central bright source. As a result, the observation exposure times are sometimes lower than those of the RGs. The bright core is difficult to model, especially if it is piled up, so that extended emission may be simply hidden, rather than nonexistent. We cannot rule out the possibility that quasars at high redshift may inhabit less rich environments than radio galaxies as most of the quasars upper limits are in the low-luminosity part of the L_X distribution.

In the top panel of Figure 2 we show the distribution of the bolometric X-ray luminosity as a function of the isotropic radio luminosity as measured at 178 MHz. We find no significant correlation between the two quantities for either the radio galaxies and the quasars.

We also find no significant correlation between the bolometric X-ray luminosity and redshift (Figure 2, middle), although a peak may be present around $z = 0.6$. To explore the evolution of the luminosity function of clusters around powerful radio-loud active galaxies it would be necessary to compare the objects drawn from this sample with objects from a broader redshift range; this would allow us to search for correlations between X-ray luminosity and redshift.

We also looked for a correlation between the extent of the gas distribution and the X-ray luminosity. The full-width-half-maximum (FWHM) of the β model describing the intra-cluster medium (ICM) distribution is

$$r_{\rm FWHM} = 2\, r_{\rm c} \times (0.5^{\frac{2}{1-6\beta}} - 1)^{1/2} \qquad (2)$$

where $r_{\rm c}$ is the core radius. Figure 2, bottom, shows that for the objects for which fitting of the radial profile was possible there is no statistically significant correlation between the FWHM of the gas distribution and its bolometric luminosity. However, the radio galaxies are preferentially found towards the right side of the plot, and there is a trend of an inverse correlation between the two quantities. This result may be an indication that radio galaxies tend to lie in more spatially extended clusters, although this does not imply richer environments, as RGs occupy the whole L_X range in the plot. Speculatively, this plot may suggest either that more luminous clusters are more concentrated, or that, for the most luminous clusters, we are only detecting their central, denser and thus more luminous part.

Table 5. Physical parameters. Col. 1: source 3CRR name; Col. 2: Central proton density; Col. 3: Central pressure of the external medium; Col. 4: average distance of the radio lobe from the centre of the source (and cluster). This is the distance used to calculate the external pressure at the location of the lobe; Col. 5: External pressure of the environment at the location of the lobe. This should be considered as an average value; Col. 6: IC minimum (equipartition) internal pressure Col. 7: IC internal pressure when it was possible to measure it from X-ray observations (see Croston et al. 2005b)

| Source	n_0 $(\times 10^{-2}$ cm$^{-3})$	P_0 $(\times 10^{-12}$ Pa$)$	Rlobe (arcsec)	P_{ext} $(\times 10^{-12}$Pa$)$	$P_{int_2}^{min}$ $(\times 10^{-12}$ Pa$)$	P_{IC} $(\times 10^{-12}$ Pa$)$
3C 6.1	< 0.6	< 4.3	8.4	< 3.5	3.1	–
3C 184	$0.5^{+0.3}_{-0.2}$	$6.4^{+4.2}_{-2.5}$	2.5	$6.3^{+4.1}_{-2.5}$	72.0	384.0 ± 115.0
3C 200	$4.8^{+3.5}_{-2.6}$	$68.45^{+49.35}_{-36.53}$	9.5	$9.9^{+1.8}_{-3.6}$	0.5	0.58 ± 0.07
3C 207	$3.8^{+13.0}_{-1.3}$	$68.50^{+2380}_{-24.31}$	4.8	$38.5^{+3.5}_{-6.8}$	2.7	3.9 ± 0.6
3C 220.1	$10.8^{+20.0}_{-5.8}$	$183.0^{+157.0}_{-85.0}$	12.0	$17.6^{+1.8}_{-1.6}$	0.8	–
3C 228	$1.1^{+10.3}_{-0.9}$	$15.15^{+145.9}_{-12.9}$	18	$3.5^{+0.8}_{-1.5}$	1.0	–
3C 254	$16.9^{+13.9}_{-7.8}$	$95.3^{+78.2}_{-44.0}$	7.5	$6.5^{+0.5}_{-0.5}$	4.0	–
3C 263	< 2.4	< 44.0	18.0	< 10.0	1.0	2.6 ± 0.5
3C 265	$6.7^{+13.9}_{-4.0}$	$25.7^{+53.2}_{-15.2}$	19.5	$0.08^{+0.2}_{-0.05}$	0.8	0.9 ± 0.1
3C 275.1	< 1.1	< 4.04	5.8	< 2.5	2.1	2.5 ± 0.3
3C 280	< 0.9	< 16.18	5.5	< 12.1	8.0	12.3 ± 3.1
3C 292	$0.9^{+0.7}_{-0.4}$	$6.8^{+5.9}_{-2.9}$	37.5	$1.1^{+0.2}_{-0.1}$	0.8	–
3C 295	12.7 ± 0.6	220 ± 10	2.0	170 ± 10	100	–
3C 309.1	$13.53^{+135.2}_{-10.2}$	$43.5^{+435.3}_{-33.2}$	–	–	–	–
3C 330	$1.3^{+3.0}_{-0.7}$	$7.7^{+17.7}_{-3.9}$	18.0	$1.2^{+0.2}_{-0.2}$	1.7	2.3 ± 0.4
3C 334	< 1.0	< 3.63	16.1	< 4.9	0.7	0.9 ± 0.4
3C 345	0.9	< 6.5	–	–	–	–
3C 380	1.3	< 9.2	–	–	–	–
3C 427.1	$2.2^{+0.6}_{-1.3}$	$45.0^{+13.0}_{-26.0}$	7.5	$13.8^{+2.3}_{-2.1}$	3.3	3.7 ± 0.6
3C 454.3	< 4.9	< 18.1	–	–	–	–
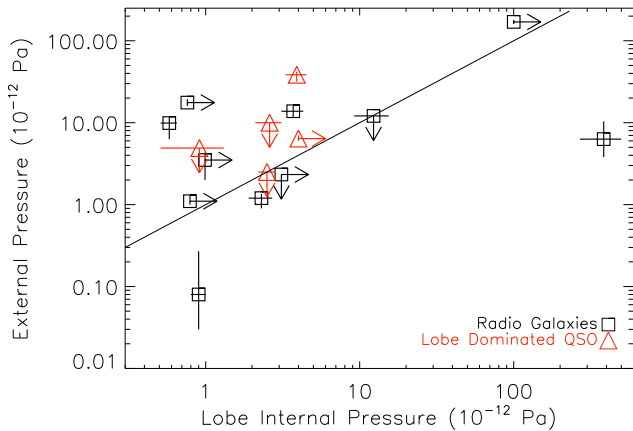
Figure 3. External (cluster) pressure at a position corresponding to the average distance of the radio lobe from the cluster centre versus total internal pressure calculated from an X-ray component of CMB inverse-Compton scattered emission in the lobe where measured, or the minimum pressure (Croston et al. 2005b). The continuous line indicates equality between external and internal pressure.

6   THE STATE OF THE RADIO SOURCE

We computed the central density, central pressure and the pressure at the location of the lobe using the best fit β model and the temperature that characterise the sources in the sample. Whenever only upper limits of the gas distribution were available, we calculated 3σ upper limits for central density and pressure. We used the relation given in Birkinshaw & Worrall (1993) to derive central proton density and pressure from the central count density. Results are tab-

ulated in Table 5. The pressure of the external environment was calculated at (or at times extrapolated to) a distance corresponding to half the distance between the centre and the edge of the radio lobe (sometimes terminating in a hot spot). This should account for the fact that radio lobes have a cylindrical shape so the pressure at the cylinder edges is a function of the gas pressure and so the distance from the centre of the cluster.

The internal pressure of the radio source was calculated by combining X-ray (IC) and radio data for those sources with detected X-ray emission from the radio lobes (Croston et al. 2005b, for details). For all other sources minimum pressures were computed using the radio data only. The IC and minimum internal pressures were obtained using the code of Hardcastle, Birkinshaw, Worrall (1998b), using the radio and X-ray flux measurements, lobe volumes, and electron energy model parameters for each source given in Croston et al. (2005b). For CDQs we are unable to calculate the radio source pressure as the jet dominates the X-ray and radio emission (see Sec. 3.2) and they are thus ignored in this analysis. In Figure 3 we plot the external, thermal gas pressure versus the internal pressure of the radio lobes. Minimum pressures are treated here as lower limits. The continuous line shows the equality of internal and thermal pressure.

Most of the sources appear to be close to pressure balance, with only a few exceptions. The source at the far right edge of the plot is 3C 184 whose size is very small (only few arcsec). We have argued in Belsole et al. (2004) that the size and relative pressure of this source suggest that it may be in a young phase and beginning to expand into the external medium (see also Siemiginowska et al. (2005) for a similar conclusion about 3C 186). 3C 265 also has lobes that are over-pressured with respect to the external gas. The sources that appear to have lobe pressures that are significantly lower than the pressure of the ICM are 3C 200, 3C 207, 3C 220.1 and 3C 427.1. The radio lobe pressure of 3C 220.1 is a lower limit (minimum pressure) so the real pressure can be higher and in agree-

ment with pressure equilibrium. 3C 207 has a bright core and caution should apply as the measurements of external pressure may have a larger than statistical error due to additional contamination of the extended environment by the point source. The remaining sources are the two low-excitation RGs (LERG) in the sample and their lobes appear genuinely under-pressured with respect to their environments. As lobes cannot evolve to a state where they are truly underpressured, this suggests that our pressure estimates for these sources may be incorrect.

Earlier evidence has suggested that LERGs prefer richer environments than high-excitation objects (e.g., Hardcastle 2004; Reynolds, Brenneman & Stocke 2005). Our result suggest that even at high redshift, powerful LERGs appear to inhabit rich environments. The behaviour of their nuclei, both from an optical/infrared and X-ray perspective, appears more similar to that of less powerful FRI radio galaxies, which are almost all LERGs. The X-ray properties of the cores of 3C 200 and 3C 427.1 (Belsole et al. 2006) are definitively consistent with this picture.

It is well known that the minimum pressures in the lobes of low-power FRI sources are almost always found to be lower, often by an order of magnitude or more, than the external pressures estimated by observations of hot gas (e.g. Croston et al. 2003; Dunn, Fabian & Celotti 2006), requiring either significant departures from equipartition in the lobes or, more likely, a dominant contribution to the lobe pressure from non-radiating particles. Our results point to the intriguing possibility that some high-power LERGs may resemble low-power sources in this respect as they do in their nuclear properties. This would imply that in fact the work done by the radio source on the environment is higher than that measured from radio observations alone (i.e. minimum energy). Thus, in contrast with what we and others have found to be the case for narrow-line radio galaxies and quasars, for the two LERGs in our sample we have measurements of the IC from X-ray observations (Croston et al. 2005b). We still observe the sources to be over-pressured by their environments, even though the measure we have of their energy density is more realistic than minimum energy.

There is evidence that some other LERG FRII sources have minimum lobe pressures that lie substantially below the external thermal pressures (e.g. 3C 388, Kraft et al. 2006; 3C 438, Kraft et al. 2007) but this is the first time that we have been able to use inverse-Compton constraints to show that the radiating particles and associated magnetic field cannot provide the required pressures: it is most likely that the 'missing' pressure in these two sources is provided by non-radiating particles such as protons.

With only two sources we cannot make a general statement, but observations of more LERGs at relatively high redshift would be beneficial to understand this dichotomy.

7 ARE RADIO GALAXY CLUSTERS DIFFERENT FROM OTHER CLUSTERS?

We have searched for any difference between X-ray clusters around radio galaxies and clusters selected with a different technique. We plot in Figure 4 the luminosity-temperature relation for the objects in our sample. The dashed line shows the best-fitting correlation for an optically selected sample of clusters from Holden et al. (2002). Errors on both luminosity and temperature for the sources in our sample are large, but we do not observe a particular trend in the relation, and most of the sources appear in agreement (within the uncertainties) with the $L_X - T$ relation valid for other clusters at the same redshift and also with the $L_X - T$ relation of local clusters
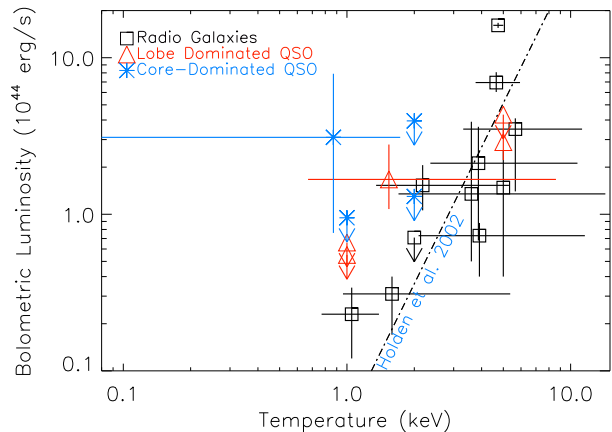

Figure 4. Luminosity-Temperature relation. The line is the best fit for a sample of optically selected clusters at $z \sim 0.8$; from Holden et al. (2002). Symbols are as in Fig. 2

(e.g. Arnaud & Evrard 1999) once the redshift dependence is taken into account. We observe that most of the quasars lie to the left of the plot. Most of the data points are upper limits, so that it is difficult to draw strong conclusions from this result. However, the position of the quasars may also indicate that the high brightness of these sources with respect to their temperature may be due to our detection of the central part of the cluster only. Since the nuclei of these sources are brighter than those of radio galaxies, it is possible that with the current data we are detecting only the central, denser and cooler region of a more extended cluster, i.e. the cooling core region.

Contrary to expectations, we do not find any source to be too hot for its luminosity. This is in contrast with results obtained for lower redshift radio sources, particularly in groups (e.g., Croston et al. 2005a). However the clusters we detect tend to have relatively high temperatures and thus with the statistics available for such high redshift sources it is not surprising that any possible effect of heating of the ICM by the radio source is hidden or masked by the poor statistics. On the other hand, we find that a few sources are overluminous for their temperature. We believe that this is more likely to be the effect of detecting only the central part of the cluster, which may be highly luminous because of its high density (cooler regions). Clusters at lower redshift, for which statistics allow the separation of the cooling region, have been found to be less luminous once the effect of the cooling flow is corrected for (e.g. Markevitch 1998; Gitti et al. 2007).

8 THE ENVIRONMENTS OF HIGH-REDSHIFT SOURCES AND THE LAING-GARRINGTON EFFECT

The Laing-Garrington effect (Laing 1988; Garrington et al. 1988), in which the lobe with the brighter or only jet appears less depolarized at GHz radio frequencies, has been attributed since its discovery to a 'hot halo' around the powerful radio sources in which the effect was first seen. The standard interpretation (Garrington & Conway 1991) is that the counterjet side, which in beaming models is the side further away from us, is seen through more of the hot gas in the group or cluster environment. As a result small-scale magnetic field variations in the hot gas give rise to unre-

solved or partially resolved (e.g. Goodlet & Kaiser 2005) Faraday rotation structure and therefore 'beam depolarization' in the low-resolution images typically used to study the effect. If a β model describes the hot gas in the system, Garrington & Conway (1991) show that the core radius of the cluster must be comparable to the size of the radio sources (i.e. ~ 100 kpc) for a significant Laing-Garrington effect to be observed. Thus observations of the Laing-Garrington effect essentially predict the existence of cluster-scale X-ray emission in the source concerned. We are now in a position to compare that prediction with the results of X-ray observations.

Laing-Garrington effect detections are only possible in sources with detected kpc-scale jets, which represent only a fraction of the objects in our sample. Of these, not all have depolarization measurements in the literature. The sources with reported Laing-Garrington effect detections in our sample are 3C 200 (Laing 1988), 3C 207 (Garrington, Conway & Leahy 1991), 3C 228 (Johnson, Leahy & Garrington 1995), 3C 275.1 (Garrington et al. 1991) and 3C 334 (Garrington et al. 1991). Of these only one (3C 200) has an environment with well-characterised spatial properties (Table 3) but these are at least qualitatively consistent with expectations: the core radius is comparable (within the large errors) with the ~ 10 arcsec lobe length. From Laing (1988), using the results of Garrington & Conway (1991), we can calculate the Faraday dispersion, which we can compare to the simple model of Garrington & Conway (1991) using our best-fitting parameters for the 3C 200 environment. The ratio of the Faraday dispersions for the measured core radius requires the source to lie at a relatively large angle to the line of sight (see figure 7 of Garrington & Conway 1991), which seems unlikely given its very one-sided jet (e.g. Gilbert et al. 2004). However, the large errors on the core radius mean that smaller angles can be accommodated by the data. Setting this aside, the best-fitting parameters for the hot gas can reproduce the lobe and counter-lobe Faraday dispersion in the Garrington & Conway model if the magnetic field strength in the gas is about 0.5 μG (0.05 nT).

Faraday dispersions in the other lobes with Laing-Garrington measurements have comparable values, so we might expect roughly similar environments for these objects. The two other sources with cluster detections, 3C 207 and 3C 228, both seem to reside in comparable environments – 3C 207's is rather more luminous but may well be less centrally peaked than 3C 200's. However, the non-detection of environments for 3C 334 and 3C 275.1 is perhaps surprising. The spectral upper limits on the luminosities of extended emission for these sources are comparable to the detection for 3C 200 (Table 4), so the simplest explanation is that these sources do have extended thermal emission that is just below our detection threshold. There is certainly at present no gross inconsistency between the depolarization measurements and our results.

9   ENTROPY PROPERTIES

Entropy is an important quantity, since it allows us to investigate at the same time the shape of the underlying potential well of the cluster and the properties of the ICM. Entropy is generated in accretion shocks during the formation of the cluster (e.g. Tozzi & Norman 2001; Voit et al. 2003; Voit 2005; Borgani et al. 2005), but it can be modified by non-gravitational processes after the formation of the cluster itself. Much emphasis has been placed on entropy in studies of galaxy clusters, from both a theoretical (e.g. Voit et al. 2002; Voit, Kay & Bryan 2005; Muanwong, Kay & Thomas 2006, and references therein) and observational (e.g.

Ponman, Sanderson & Finoguenov 2003; Pratt & Arnaud 2005; Piffaretti et al. 2005; Pratt, Arnaud, & Pointecouteau 2006) perspective. Recent results show that entropy is higher than expected from pure gravitational models on cluster spatial scales out to at least half the virial radius (e.g. Pratt et al. 2006, and references therein) and not only in the central regions. Although the pre-heating scenario (e.g., Kaiser 1991; Evrard & Henry 1991; Valageas & Silk 1999) is now considered unlikely (e.g. Ponman et al. 2003; Pratt & Arnaud 2003, 2005), mechanisms such as heating and cooling due to more recent supernovae or AGN activity are still a viable explanation for the general excess of entropy. There is a consensus about the significant effect of feedback from a central AGN in the evolution of the ICM. An important result is that central AGNs can act not only in the central region of what were historically called "cooling flow" clusters, but also on large scales, e.g. through sonic shocks, observed as ripples in the ICM (Fabian et al. 2006) or strong shock waves (Forman et al. 2005). This is particularly relevant as the AGN hypothesis to explain the excess entropy in galaxy clusters can also apply to the large scale excess and it is not limited to the central entropy excess initially detected in cool systems (e.g. Ponman, Cannon & Navarro 1999; Lloyd-Davies, Ponman & Cannon 2000; Ponman, Sanderson & Finoguenov 2003).

These recent results on entropy motivated us to investigate the entropy properties of the clusters in our sample. Although the errors are large, this is the first time that entropy has been investigated for the ICM around radio sources at this redshift. Here we adopt the accepted definition of entropy in the X-ray:

$$S = kT/n_e^{2/3} \qquad (3)$$

In order to compare with low-redshift clusters, we scale this with redshift using the relation $S_z = h^{4/3}(z) \times S$. For the sources in the sample we are unable to produce entropy profiles as we only have a global temperature and therefore the shape of the profile would depend exclusively on the shape of the density profile. We thus only obtained global entropy properties at specific distances from the centre of the cluster.

Figure 5, left, shows the central entropy S_0 compared to the radio power at 178 MHz. The isotropic radio power is often taken to be a proxy of the jet power (Willott et al. 1999), and thus should be correlated with the power being injected into the ICM. The entropy reflects the accretion history of the cluster but also the influence of non-gravitational processes. We find that the central entropies of all the objects in the sample are similar and there is no correlation between S_0 and L_{178MHz}. We also see that RGs and quasars are scattered equally in the space defined by these two parameters, although caution should be used as regards the CDQs since their low-frequency radio emission may be contaminated by emission from the jet. The lack of correlation between the two quantities may be the result of the short life time of the radio source with respect to the cluster age; the two quantities may be unrelated because they arise from processes that take place at different epochs.

In the right-hand panel of Figure 5 we plot the entropy at 0.1 r_{200} versus the temperature of each cluster (upper limits are not shown for clarity, but symbols without error bars should be interpreted as limits). This is similar to what Pratt et al. (2006) and others have done for lower redshift clusters. In the Figure the objects in our sample are compared to a sample of 10 clusters at redshift less than 0.2 (Pratt et al. 2006). We also plot the best-fitting temperature-entropy relation for this low-z cluster sample, extrapolated to low temperatures. We observe that, at 0.1 r_{200}, clusters around RGs with temperature above 2.5 keV appear similar in their
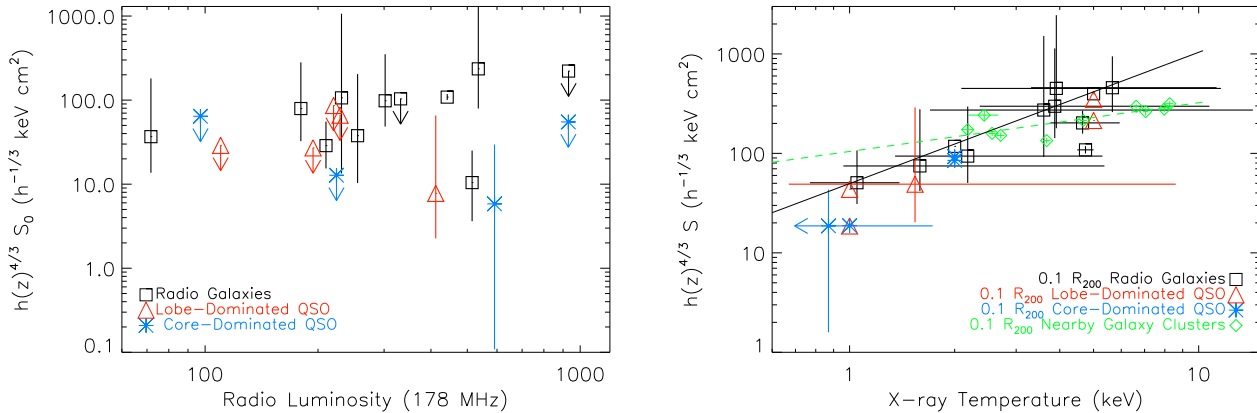
Figure 5. Left: Central entropy versus the radio power of the source at 178 MHz. We used the best-fitting temperature when available and otherwise took a fixed value when the data were not of good enough quality to perform spectral fitting. Right: Entropy calculated at $0.1\ r_{200}$ as a function of the cluster temperature. Errors are not shown when the temperature used to fit the spectrum was a fixed parameter. (The only exception is for 3C 309.1, where the arrow does not represent a limit but is used to show that the lower boundary of temperature error is beyond the scale of the plot.) The red diamonds are clusters at redshift < 0.1 and with temperatures between 2.9 and 10 keV, from Pratt et al. (2006). The dashed line is the best fit to the cluster sample only, extrapolated to low energy. In the centre and bottom figure the entropy S has been scaled for redshift as $S_z = h(z)^{4/3} \times S$, where h(z) = $(\Omega_m \times (1+z)^3 + \Omega_\Lambda)^{0.5}$

entropy properties, within the uncertainties, to clusters at lower redshift. However they are preferentially found above the best-fitting temperature-entropy relation for local clusters, suggesting that they have a larger amount of entropy than their local counterpart. The cooler radio-galaxy clusters all lie below the local $S - T$ relation of Pratt et al. , and although we do not show it here, our data cannot be fitted by the best-fit $S - T$ relation of slope 0.65 found by Ponman et al. (2003) using a sample of local groups, galaxies and clusters, which may be a more appropriate comparison for the low-temperature systems in our sample. We have calculated the entropy at $0.5\ r_{200}$ and the trend is similar. However, in many cases calculation of the density at this radius requires a large extrapolation from the data so that the results may be biased.

Using the ASURV package (Isobe et al. 1990) to account for censored data, we find that the relationship between $S\ (0.1\ r_{200})$ and T is fitted by a relation of slope 1.32±0.22, in reasonable agreement with what is expected from self-similar models (slope of 1; Ponman et al. 1999) – note that errors here are 1σ. This seems to suggest that there is less entropy in high-redshift cool systems than their local counterparts, which is the opposite of what is expected if, as observed for larger sample of galaxy groups and clusters, the cool systems are more strongly affected by feedback processes. It also appears counter-intuitive given the presence of a powerful radio source at the centre of all our clusters. However, the presence of the radio source may represent a concrete explanation for this behaviour. The AGN (at least for the conventional AGN that dominates our sample) needs to be fuelled to be activated and for the accretion to be radiatively efficient, as is the case for most of the sources in the sample (see Belsole et al. 2006), it needs the accreted gas to be relatively cold. The required cool gas becomes available when low-entropy gas is present close enough to the accretion region. For this to happen, it is commonly accepted that the cluster must be in a virialized state. Since the cluster requires a time which is much longer than the lifetime of synchrotron emitting electrons at 1.4 GHz ($\sim 10^8$ yrs) to relax, the radio sources in this sample may be in a state in which the energy of the outburst due to the AGN activation has not yet been transferred to the ICM, even in the cen-

tral region. Clusters at lower redshift, such as those in Pratt et al. (2006) or groups (Ponman et al. 2003) have had more time for the distribution of AGN energy output throughout the cluster, and their high entropy level, especially within $0.1\ r_{200}$, may be the effect of repeated outburst. If we accept the interpretation of cyclic activation of the central supermassive black hole, the duty cycle must be higher in low-redshift clusters. It is possible in our present sample that we are witnessing the first activation of a radio galaxy at the centre of a dense cluster-like environment, particularly bearing in mind that the 3CRR sources on which our sample is based are at the top end of the luminosity function and are rare at all epochs. This may also be interpreted as suggesting that the duty cycle of more luminous radio sources is much lower than that of less active AGN. In other words, the sources in the sample with low central entropy may be selected to be those in which the effect of the radio source is not yet observable in entropy, but will be in the future.

If this result can be confirmed with better statistics, and/or the larger samples that will be available with X-ray instruments such as *XEUS*, it may give important constraints on the overall mechanism of AGN heating of the ICM, entropy distribution in large scale structure and, last but not least, the formation, evolution and ageing of radio sources in dense environments.

10 CONCLUSIONS

We have analysed X-ray data from *Chandra* and *XMM-Newton* of 20 powerful RGs and quasars at redshift $0.45 < z < 1$ with the aim of investigating their external environment and its interaction with the bright radio source. We find that:

(i) RGs and quasars inhabit a range of environments without any obvious relationship to radio properties such as radio power and size.

(ii) more than 60 per cent of the sources lie in X-ray emitting environments of luminosity greater than 10^{44} erg s^{-1}. The poorest environments in this redshift range are consistent with moderate-

luminosity groups ($L_X \sim 10^{42}$ erg s^{-1}), the richest with Abell class 2 ($L_X > 5 \times 10^{44}$ erg s^{-1})) or above clusters.

(iii) Our results are in agreement with unification schemes that predict that the environment of sources oriented with various angles to the line of site should be isotropic. Most of the objects whose jet is oriented close to the plane of the sky (RGs) are detected to lie in rich environments while for 6 out of 9 quasars we are able to estimate upper limits for the existence of a cluster-like component around them. These upper limits occupy the same parameter space of luminosities as the detected sources. Seven of the sources are found to be point-like. However three of them are core-dominated quasars for which the detection of a low-surface brightness X-ray component is hampered by the bright X-ray core emission.

(iv) Within the uncertainties, these are normal environments, with no evidence that they deviate from the temperature/luminosity relationship observed in low-z normal clusters. Therefore there is no strong evidence that the presence of a radio source requires a peculiar environment or strongly affects the cluster. This may also suggest that deviation from self similarity and the scatter around scaling laws is likely to be affected by other processes such as mergers (Maughan 2007), rather than the interaction between the radio source and the central cluster.

(v) For the first time for radio active sources at this redshift we investigate the entropy of the ICM. To our surprise we find that the entropy/temperature relation is steeper than that observed for low-redshift normal galaxy clusters, and closer to the relation predicted by self-similar models. We argue that this is the result of processes occurring at different epochs, the intensity of the AGN duty cycle at low and high redshift, and that the heating from the radio source outburst may have not have had the time yet to be observed in the ICM entropy for sources at redshift above 0.5.

(vi) Most of the sources appear close to pressure balance with the cluster, with the exception of the two LERGs in the sample which appear under-pressured. Although measurements of the internal pressure are still uncertain, this comparison is more precise than using simple minimum pressures from radio data. The result on LERGs may be the first evidence of the presence of non-radiating particles that contribute to the radio source internal pressure in powerful radio sources.

APPENDIX A: NOTES ON INDIVIDUAL SOURCES

In this Appendix we describe details of the source-specific analysis for each of the sources in the sample. For each source we show wavelet-decomposed images in the soft (0.5-2.0 keV) and hard (2.5-7.0 keV) energy bands, together with the radial profile fitting described in the text, with both a PSF alone and a PSF plus β-model when required. The fitting results for radial profile and spectral analysis are in Tables 3 and 4. The images and profile can be inspected in Fig. A1-A18. The contours in the images are from VLA data at 1.4 GHz, except where otherwise stated. No radio overlays are shown for the 4 CDQs due to the small size of the source (see also Sec. 3.2).

• **3C 6.1:** The radial profile is well fitted with a PSF only and there is no significant improvement in the fit if an extra component is added. We fix the β parameter to 0.5 and the core radius r_c to 15 arcsec = 115 kpc, for a 2 keV cluster, which is a typical r_c value for a cluster in the local universe (~ 125 kpc). We calculate a 3σ upper limit for any cluster-like extended emission with these parameters.

We extracted the spectrum in the same source and background area as used for the radial profile. We fitted the spectrum with 1) a power law absorbed by Galactic absorption and 2) a thermal model. We find a similar goodness of fit. The power-law slope is found to be 1.7 ± 0.5 when the spectrum is fitted between 0.5-2.5 keV and 1.4 ± 0.23 if the 0.5-6.0 keV band is used. Both are consistent with the spectrum being due to the wings of the PSF. However, the number of counts does not correspond to what is expected from the wings of the PSF at the distance from the centre we use (a circle of radius 5-arcsec was used to mask the central unresolved point source). The source is only slightly piled-up. The other option for the nature of this extended emission may be IC from the region coincident with the radio lobes or the hotspots. However those areas were masked prior to spectrum extraction, and Croston et al. (2005b) find only upper limits for the IC emission from the lobes. For this reason, we evaluated the luminosity of the emission detected in the circle of radius 49.2 arcsec used for the spectral analysis by fixing a temperature of 2 keV and assuming it to be thermal. Images of 3C 6.1 are in Figure A1.

• **3C 184** This source was analysed in detail by Belsole et al. (2004). The point source is not spatially separated from the extended emission with the *XMM-Newton* data, and 20 ks are not sufficient to detect cluster emission with *Chandra*. However, the *XMM-Newton* spectrum is best fitted with 3 components, one of which is a MEKAL with at best-fit temperature of $\sim$3.6 keV. Images and profiles can be inspected in Belsole et al. (2004).

• **3C 200:** This is a low-excitation radio galaxy, so the core is faint with respect to the lobe emission, making the investigation of diffuse emission easier. The statistics are good enough to constrain the radial profile and spectral parameters. Figure A2 shows images for this source.

• **3C 207:** There are a total of 190 net counts in the region used for the spectral analysis: a circle of radius 15 arcsec with the exclusion of a circle of radius 5 arcsec to mask the core, and areas to mask the western lobe and jet. The spectrum can be fitted with a simple power-law model of slope 1.15, giving a χ^2/d.o.f = 3.06/4. There is no statistically significant need for a thermal component in agreement with Brunetti et al. (2002) and Gambill et al. (2003). However, the radial profile analysis strongly suggests the presence of an extended component with a King profile distribution and standard parameters. We thus calculated the fraction of counts from the wings of the PSF expected in the area used for the spectral analysis, and we derived the normalisation of the power law model in this area. We then fixed the value of Γ to be equal to the lower limit of Γ found while fitting the core spectrum. This is justified by the flattening of a point source spectrum in the PSF wings. Finally we assumed that the rest of the counts were from extended, cluster-like emission that was fitted with a MEKAL model of fixed temperature 5 keV. Given the uncertainties of the spectral fitting, we have assigned the source a quality flag of D (detection only) despite the fact that β model parameter are well constrained. These results should thus only be regarded as giving one plausible scenario. Using the same data Brunetti et al. (2002) interpret most of the X-ray emission surrounding one of the lobes as non-thermal; however, they do not exclude the possibility that a low-surface brightness cluster may be present.

• **3C 220.1:** This source was detected previously with *ROSAT* (Hardcastle, Lawrence, Worrall 1998a) and using the same *Chandra* data by Worrall et al. (2001). It is one of the best examples of a rich cluster around a radio galaxy in this redshift range, and the precision of physical parameters obtained from spatial and spectral analysis are comparable to X-ray clusters in the local universe. Our results are in perfect agreement with previous studies of this cluster.

• **3C 228:** Two exposures for this source give a total of ~ 24 ks

Figure A1. From left to right: Soft (0.5-2.0 keV) and hard (2.5-7.0 keV) wavelet-decomposed image for 3C 6.1. Contours are from a 1.4-GHz radio map (A configuration, L band) and are logarithmically spaced. Radial profile fitted with a simple PSF. The β-model fitting of the radial profile is not shown as only an upper limit was calculated.

Figure A2. From left to right: Soft (0.5-2.0 keV) and hard (2.5-7.0 keV) wavelet-decomposed image for 3C 200. Contours are from a 1.4-GHz radio map (B configuration, L band) and are logarithmically spaced. Radial profile fitted with simple PSF and a PSF plus a β-model.

of flare-clean *Chandra* observation. This allows us to explore the β-r_c parameter space but not to constrain the two parameters. The point source dominates the X-ray emission out to 6 arcsec and this was excluded prior to spectrum extraction. We thus fixed the β and r_c to 0.5 and 15 arcsec respectively and only calculated errors on the normalisation.

The spectrum is well fitted with a MEKAL model of $kT = 3.9$ keV and metallicity 0.3 solar. However it can also be fitted with a power law of $\Gamma = 1.8$. The two fitted models are statistically equivalent; however, the nucleus of the source has a flatter ($\Gamma = 1.6 \pm 0.1$) spectrum, so that this emission is unlikely to come from the wings of the PSF. IC emission from the radio lobes may be the other source of uncertainty but Croston et al. (2005b) only find upper limits on IC flux from the radio lobes. We thus assume that a thermal model describing the external environment is the most likely interpretation for the X-ray emission detected by our spectral analysis.

• **3C 254:** The radial profile of 3C 254 is dominated by the PSF out to 40 arcsec. This is one of the significantly piled up sources, with a pileup fraction of 20 per cent. However, for both the radial profile and the spectral analysis, the PSF alone is not sufficient to account for all the X-ray emission and we constrain the shape (β model) and spectral parameters. From the best fit r_c value the object appears rather compact and the low temperature we find may suggest that we have possibly detected the galaxy atmosphere rather than a cluster. Crawford & Fabian (2003) detect extended X-ray emission around 3C 254 with a luminosity in the 0.5-7 keV range of $(3.1 \pm 1.2) \times 10^{43}$ erg s^{-1}, which is in agreement with what we find within the errors.

• **3C 263:** The source is heavily piled up. We used the piled up PSF model to characterise the point source distribution. However, given the uncertainties of this model for heavily piled up sources, we cannot account for all the residuals and the fit is not good. The addition of a β-model improves the fit but the parameters we find are not physical, and suggest a best-fit value for the core radius close to zero. We interpret this result as the effect of our poor modelling of the wings of the PSF for a heavily piled up source. As a result, we fix β and r_c to canonical values and obtained upper limit only from both the radial profile and spectrum.

Crawford & Fabian (2003) and Hardcastle et al. (2002) previously studied this source and they both claimed detection of cluster emission, albeit of low surface brightness. However their modelling of the PSF did not take pileup into account and their result may be due to pollution from the point source, although 3C 263 seems to lie in a spectroscopically confirmed optical cluster (Hall et al. 1995). To summarize, it may be possible that a cluster exists around 3C 263, but given the poor fitting results we obtain we adopt the safe solution and use upper limits only for this source.

• **3C 265:** The upper value of the β parameter was not constrained, which can be explained as the result of the poor statistics for this object, mostly due to the large mask used to exclude the radio lobes. The relatively low temperature we measure suggests

that the source lies in a group or that we are detecting only the very centre of a larger cluster which may have a cool core.

• **3C 275.1** The radial profile and the spectral analysis both indicate that the X-ray emission is from a point source. We thus carried out upper limit calculation for the existence of a cluster component. This is not in agreement with what was found by Crawford & Fabian (2003) who detected a cluster of bolometric X-ray luminosity $7.6 \pm 0.9 \times 10^{43}$ erg s^{-1}.

• **3C 280:** The β-model parameters are not constrained. However, there is a significant improvement over a PSF model alone if an extended model is added. We use here the best-fitting parameters of the β model to characterise the extended emission: the derived values should therefore be used with caution. Similarly, the count statistics of the current *Chandra* observation do not allow us to constrain the temperature, although the spectrum is better fitted with a thermal model than a power law. The luminosity we measure is within the upper limit of Donahue, Daly & Horner (2003), although we claim a detection.

• **3C 292:** Belsole et al. (2004) give a detailed analysis of this source.

• **3C 295:** This rich cluster was previously studied by Allen et al. (2001) using a *Chandra* ACIS-S observation. We have used a more recent 90-ks observation made with the ACIS-I detector. These data have extremely good statistics and would allow a much more detailed analysis of the source than we have presented here. For consistency, however, we have analysed 3C 295 in the same way as all the other sources. The host cluster of 3C 295 is the most luminous cluster around a 3CRR source in the redshift range of the paper. Our morphological analysis agrees with what was found by Allen et al. Since we calculate a global temperature for the cluster, we find a slightly lower temperature than Allen et al. , who exclude the cooling flow region. For the same reason, 3C 295 appears too luminous for its temperature (see Fig. 4). However, if we accept the measurements of Allen et al. beyond 50 kpc, the source is found more in line with the $L_X - T$ relation shown in Fig. 4. Despite being an extreme case in our sample (because of the number of X-ray counts detected and high luminosity), 3C 295 appears similar to the other 3CRR sources in the 0.45–1 redshift range when its global properties are considered.

• **3C 309.1:** This is the only core-dominated quasar for which we have been able to estimate the extent of the thermal emission. The source was observed with a small window and thus only the area covered by the detector was used. A King profile in addition to the PSF is required to fit the radial profile of 3C 309.1, and the shape of the profile is constrained. In order to increase the S/N ratio we reduced the area for extraction of the spectrum to a circle of radius 32 arcsec (instead of r = $\sim$ 40 arcsec used for the radial profile). The bright point source was masked by a circle of radius 9 arcsec, thus reducing considerably the contamination of the PSF, even for a piled up source. The readout streak was also masked. The low number of counts in this region (60 net counts) requires the use of Cash statistics. Although a power law gives an accept-

Figure A3. From left to right: Soft (0.5-2.0 keV) and hard (2.5-7.0 keV) wavelet-decomposed image for 3C 207. Contours are from a 1.4-GHz radio map (A configuration, L band) and are logarithmically spaced. Radial profile fitted with simple PSF and a PSF plus β-model.

Figure A4. From left to right: Soft (0.5-2.0 keV) and hard (2.5-7.0 keV) wavelet-decomposed image for 3C 220.1. Contours are from a 1.4-GHz radio map (B configuration, L band) and are logarithmically spaced. Radial profile fitted withe simple PSF and a PSF plus β-model.

able fit for the spectrum, the slope is too steep ($\Gamma = 2$), and it is not in agreement with the spectrum of the point source. The spectrum of 3C 309.1 is better fit with a MEKAL model of low temperature ~ 0.9 keV, even though the statistical errors are large. Therefore, spatial and spectral data both seem to indicate that this object lies in a X-ray emitting external environment. With the current data we cannot say whether our detection corresponds to a galaxy group, a bright elliptical galaxy or the centre of a cooling core cluster atmosphere and additional observations of this source would help to shed light on the nature of its environment.

• **3C 330:** The *Chandra* data allow us to fully determine the spatial and spectral characteristics of this source. Our results are in agreement with those of Hardcastle et al. (2002).

• **3C 334:** The radial profile is well modelled with a PSF accounting for pileup. The spectral distribution suggests that if a thermal component is present, it is relatively cold as the 20 net counts left after excluding the core emission are below 1 keV. We thus fixed the temperature to be 1 keV and calculated a 3σ limit for the presence of an extended environment.

• **3C 345:** The radial profile is modelled with a PSF, accounting for pileup. We fix the temperature of any thermal component to 2 keV to estimate the upper limit of thermal emission from the spectrum.

• **3C 380:** Like 3C 345, 3C 380 is a core-dominated quasar for which the modelling of the PSF is complicated by pileup. The radial profile is well fitted with a PSF model and upper limits are evaluated for the existence of an extended thermal component using our standard values for β and r_c and assuming a temperature of 2 keV.

• **3C 427.1:** This source is a LERG with a very weak nucleus. The emission extends out to a radius of 200 kpc and is thermal in nature, with a best-fit temperature of 5.7 keV. Using the radial profile we can only map the extended emission out to 25 per cent of the virial radius and there may be some indication that a secondary β model is needed to fit the profile, but its parameters are not constrained. Croston et al. (2005b) did not detect significant counts from the radio lobes. Nevertheless, we applied a conservative approach and excluded the spatial areas coincident with the radio lobes when extracting both spectrum and radial profile. The thermal model fit gives an interestingly high temperature for a source at this redshift. The Fe K$_\alpha$ line appear very strong. If the chemical abundance is left as a free parameter, the best fit give $Z/Z_\odot = 1.68$, and 1σ errors suggest that it is a greater than 0.76 (although the upper limit is found to be 3.8. We thus decided to fix $Z/Z_\odot$ to 1 and fit with this parameter frozen. A power-law model gives a worse fit but not significantly so ($\Delta\chi^2 = 2.5$) and a best fit of $\Gamma = 1.6 \pm 0.2$.

• **3C 454.3:** Even though the radial-profile fit using a piled-up PSF shows significant residuals, we interpret this as the effect of a poor modelling of the pileup rather than the detection of a secondary component. As a result, for this core-dominated quasar we calculate 3σ upper limits for the presence of an extended and thermal (1 keV) environment.

REFERENCES

Allen, S. W., et al., 2001, MNRAS, 324, 842
Arnaud, K. A., Fabian, A. C., Eales, S. A., Jones, C., Forman, W., 1984, MNRAS, 211, 981
Arnaud, M., Evrard, A.E., 1999, MNRAS, 305,631
Arnaud, M., Pointecouteau, E., Pratt, G. W., 2005, A&A, 441, 893
Begelman, M. C., Blandford, R. D., Rees, M. J., 1984, RvMP, 56, 255
Belsole, E., Worrall, D. M., Hardcastle, M. J., Birkinshaw, M., Lawrence, C. R., 2004, MNRAS, 352, 924
Belsole, E., Worrall, D.M., Hardcastle, M.J., 2006, MNRAS, 366, 339
Best, P. N., 2004, MNRAS, 351, 70
Birkinshaw, M., Worrall, D.M., 1993, ApJ, 412, 568
Brunetti, G., Bondi, M., Comastri, A., Setti, G., 2002, A&A, 381, 795
Borgani, S., Finoguenov, A., Kay, S. T., Ponman, T. J., Springel, V., Tozzi, P., Voit, G. M., 2005, MNRAS, 361, 233
Bower, R. G., Smail, I., 1997, MNRAS, 290, 292
Carilli, C. L., Harris, D. E., Pentericci, L., Röttgering, H. J. A., Miley, G. K., Kurk, J. D., van Breugel, W., 2002, ApJ, 567, 781
Celotti, A., Fabian, A.C., 2004, MNRAS, 353, 523
Crawford, C. S., Lehmann, I., Fabian, A. C., Bremer, M. N., Hasinger, G.,1999, MNRAS, 308,1159
Crawford, C. S., Fabian, A. C., 2003, MNRAS, 339, 1163
Croston, J. H., Hardcastle, M. J., Birkinshaw, M., Worrall, D. M., 2003, MNRAS, 346, 1041
Croston, J. H., Hardcastle, M. J., Birkinshaw, M., 2005a, MNRAS, 357, 279
Croston, J. H., Hardcastle, M. J., Harris, D. E., Belsole, E., Birkinshaw, M., Worrall, D. M., 2005b, ApJ, 626, 733
Deltorn, J.-M., Le Fèvre, O., Crampton, D., Dickinson, M., 1997, ApJ, 483, 21
Dickey, J. M., Lockman, F.J ., 1990, ARA&A. 28, 215
Donahue, M., Daly, R. A., Horner, D. J., 2003, ApJ, 584, 643

Figure A5. From left to right: Soft (0.5-2.0 keV) and hard (2.5-7.0 keV) wavelet-decomposed image for 3C 228. Contours are from a 1.4-GHz radio map (B configuration, L band), and are logarithmically spaced. Radial profile fitted withe simple PSF and a PSF plus β-model.

Figure A6. From left to right: Soft (0.5-2.0 keV) and hard (2.5-7.0 keV) wavelet-decomposed image for 3C 254. Contours are from a 1.4-GHz radio map (configuration A, band L) and are logarithmically spaced. Radial profile fitted withe simple PSF and a PSF plus β-model.

Figure A7. From left to right: Soft (0.5-2.0 keV) and hard (2.5-7.0 keV) wavelet-decomposed image for 3C 263. Contours are from a 1.4-GHz radio map (configuration A, L band) and are logarithmically spaced. Radial profile fitted with a simple PSF.

Figure A8. From left to right: Soft (0.5-2.0 keV) and hard (2.5-7.0 keV) wavelet-decomposed image for 3C 265. Contours are from a 1.4-GHz radio map (configuration B, L band), and are logarithmically spaced. Radial profile fitted with a simple PSF and a PSF plus β-model.

Figure A9. From left to right: Soft (0.5-2.0 keV) and hard (2.5-7.0 keV) wavelet-decomposed image for 3C 275.1. Contours are from a 1.4-GHz radio map (A configuration), and are logarithmically spaced. Radial profile fitted with simple PSF.

Figure A10. From left to right: Soft (0.5-2.0 keV) and hard (2.5-7.0 keV) wavelet-decomposed image for 3C 280. Contours are from a 1.4-GHz radio map (A configuration), and are logarithmically spaced. The radial profile is fitted with a simple PSF and a PSF plus β-model.

Figure A11. From left to right: Soft (0.5-2.0 keV) and hard (2.5-7.0 keV) wavelet-decomposed image for 3C 295. Contours are from an 8.6-GHz radio map (A configuration), and are logarithmically spaced. The radial profile is fitted with a simple PSF and a PSF plus β-model.

Figure A12. From left to right: Soft (0.5-2.0 keV) and hard (2.5-7.0 keV) wavelet-decomposed image for 3C 309.1. Radial profile fitted with a simple PSF and a PSF plus β-model.

Figure A13. From left to right: Soft (0.5-2.0 keV) and hard (2.5-7.0 keV) wavelet-decomposed image for 3C 330. Contours are from a VLA 1.4-GHz radio map taken in configuration A, and are logarithmically spaced. Radial profile fitted with a simple PSF and a PSF plus β-model.

Figure A14. From left to right: Soft (0.5-2.0 keV) and hard (2.5-7.0 keV) wavelet-decomposed image for 3C 334. Contours are from a 1.4-GHz radio map taken in configuration B, and are logarithmically spaced. Radial profile fitted with a piled up model of the PSF.

Figure A15. From left to right: Soft (0.5-2.0 keV) and hard (2.5-7.0 keV) wavelet-decomposed image for 3C 345. Radial profile fitted with a piled up model of the PSF.

Figure A16. From left to right: Soft (0.5-2.0 keV) and hard (2.5-7.0 keV) wavelet-decomposed image for 3C 380. Radial profile fitted with a piled up model of the PSF.

Figure A17. From left to right: Soft (0.5-2.0 keV) and hard (2.5-7.0 keV) wavelet-decomposed image for 3C 427.1. Contours are from a 1.4-GHz radio map (Configuration A), and are logarithmically spaced. Radial profile fitted with a simple PSF and a PSF plus β-model.

Figure A18. From left to right: Soft (0.5-2.0 keV) and hard (2.5-7.0 keV) wavelet-decomposed image for 3C 454.3. Radial profile fitted with a piled up model of the PSF.

Dunn, R. J. H., Fabian, A. C., Celotti, A., 2006, MNRAS, 372, 1741

Eke, V. R., Cole, S. Frenk, C.S., Henry, P.J., 1998, MNRAS, 298, 1145

Evrard, A. E., 1989, ApJ, 341, L71

Evrard, A. E., Henry, J.P., 1991, ApJ, 383, 95

Fabian, A. C., Sanders, J. S., Crawford, C. S., Ettori, S., 2003, MNRAS, 341, 729

Fabian, A. C., Sanders, J. S., Taylor, G. B., Allen, S. W., Crawford, C. S., Johnstone, R. M., Iwasawa, K., 2006, MNRAS, 366, 417

Finoguenov, A., Ponman, T. J., Osmond, J. P. F., Zimer, M., 2007, MNRAS, 374, 737

Forman, W., et al., 2005, ApJ, 635, 894

Gambill, J. K., Sambruna, R. M., Chartas, G., Cheung, C. C., Maraschi, L., Tavecchio, F., Urry, C. M., Pesce, J. E., 2003, A&A, 401, 505

Garrington, S., Leahy, J.P., Conway R.G., Laing R.A., 1988, Nature, 331, 147

Garrington, S.T., Conway, R.G., 1991, MNRAS, 250, 198

Garrington, S.T., Conway R.G., Leahy J.P., 1991, MNRAS, 250, 171

Ghisellini, G., Padovani, P., Celotti, A., Maraschi, L., 1993, ApJ, 407, 65

Gilbert, G., Riley, J.M., Hardcastle, M.J., Croston, J.H., Pooley, G.G., Alexander, P., 2004, MNRAS, 351, 845

Gitti, M., McNamara, B. R., Nulsen, P. E. J., Wise, M. W., 2007, ApJ, 660, 111

Goodlet, J. A., Kaiser, C. R., 2005, MNRAS, 359, 1456

Grevesse, N., Sauval, A. J., 1998, Space Science Reviews 85, 161

Hall, P.B., Ellingson, E., Green, R.F., Yee, H.K.C., 1995, AJ, 110, 513

Hall, P.B., Green, R.F., 1998, ApJ, 507. 558

Henry, J. P., Henriksen, M. J., 1986, ApJ, 30, 689

Hardcastle, M. J., Lawrence, C. R., Worrall, D. M., 1998a, ApJ, 504, 743

Hardcastle, M. J., Birkinshaw, M., Worrall, D. M., 1998b, MNRAS, 294, 615

Hardcastle, M. J., Worrall, D. M., 1999, MNRAS, 309, 969

Hardcastle, M. J., Worrall, D. M., 2000, MNRAS, 319, 562

Hardcastle, M. J., Birkinshaw, M., Cameron, R. A., Harris, D. E., Looney, L. W., Worrall, D. M., 2002, ApJ, 581, 948

Hardcastle, M.J., 2004, A&A, 414, 927

Hardcastle, M. J., Evans, D. A., Croston, J. H., 2006, MNRAS, 370, 1893

Hill, G. J., Lilly, S. J., 1991, ApJ, 367, 1

Holden, B. P., Stanford, S. A., Squires, G. K., Rosati, P., Tozzi, P., Eisenhardt, P., Spinrad, H., 2002, AJ, 124, 33

Isobe T., Feigelson E.D., Akritas M. J., Babu J., 1990, ApJ, 346, 104

Jackson, N., & Rawlings, S., 1997, MNRAS, 286, 241

Johnson, R.A., Leahy, J.P., Garrington, S.T., 1995, MNRAS, 273, 877

Kaiser, N., 1991, ApJ, 383, 104

Kraft, R. P., Azcona, J., Forman, W. R., Hardcastle, M.J., Jones, C., Murray, S. S., 2006, ApJ, 639, 753

Kraft, R.P., Forman, W.R., Hardcastle, M.J., Jones, C., Nulsen, P.E.J, 2007, ApJ, 664, 83

Laing, R. A., Riley, J. M., Longair, M. S., 1983, MNRAS, 309, 151

Laing, R.A., 1988, Nature, 331, 149

Lloyd-Davies, E. J., Ponman, T. J., Cannon, D. B., 2000, MNRAS, 315, 689

Markevitch, M., 1998, ApJ, 504, 27

Marshall, H. L., et al., 2005, ApJS, 156, 13

Maughan, B.J., 2007, ApJ, submitted, astro-ph/0703504

Muanwong, O., Kay, S. T., Thomas, P. A., 2006, ApJ, 649, 640

Mullis, C. R., Rosati, P., Lamer, G., Böhringer, H., Schwope, A., Schuecker, P., Fassbender, R., 2005, ApJ, 623, 85

Oukbir, J., Blanchard, A. 1992, A&A, 262, L21

Piffaretti, R., Jetzer, Ph., Kaastra, J. S., Tamura, T., 2005, A&A, 433, 101

Ponman, T. J., Cannon, D. B., Navarro J. F., 1999, Nature, 397, 135

Ponman, T. J., Sanderson, A. J. R., Finoguenov, A., 2003, MNRAS, 343, 331

Pratt, G. W., Arnaud, M., 2003, A&A, 408, 1

Pratt, G. W., Arnaud, M., 2005, A&A, 429, 791

Pratt, G. W., Arnaud, M., Pointecouteau, E., 2006, A&A, 446, 429

Reynolds, C.S., Fabian, A.C., 1996, MNRAS, 278, 479

Reynolds, C. S., Brenneman, L. W., Stocke, J. T., 2005, MNRAS, 357, 381

Sambruna, R. M., Maraschi, L., Tavecchio, F., Urry, C. M., Cheung, C. C., Chartas, G., Scarpa, R., Gambill, J. K., 2002, ApJ, 571, 206

Schuecker, P., et al., 2001, A&A, 368, 86

Schuecker, P., Böhringer, H., Collins, C. A., Guzzo, L., 2003, A&A, 398, 867

Siemiginowska, A., Cheung, C. C., LaMassa, S., Burke, D. J., Aldcroft, T. L., Bechtold, J., Elvis, M., Worrall, D. M., 2005, ApJ, 632, 110

Stanford, S.A., et al., 2006, ApJ, 646, 13

Tavecchio, F., Maraschi, L., Wolter, A., Cheung, C. C., Sambruna, R. M., Urry, C. M., 2007, ApJ, 662, 900

Tozzi, P., Norman, C., 2001, ApJ, 546, 63

Valageas, P., Silk, J., 1999, A&A, 347, 1

Voit, G. M., Bryan, G. L., Balogh, M. L., Bower, R. G., 2002, ApJ, 576, 601

Voit, G.M., Balogh, M. L., Bower, R. G., Lacey, C.G., Bryan, G.L., 2003, ApJ, 593, 272

Voit, G. M., Kay, S. T., Bryan, G. L., 2005, MNRAS, 364, 909

Voit, G.M., 2005, Rev. Mod. Phys. 77, 207

Willott, C.J., Rawlings, S., Blundell, K.M., Lacy, M., 1999, MNRAS, 309, 1017

Willott, C. J., Rawlings, S., Blundell, K. M., Lacy, M., Eales, S. A., 2001, MNRAS, 322, 536

Wold, M., Lacy, M., Lilje, P. B., Serjeant, S., 2000, MNRAS, 316, 267

Wold, M., Lacy, M., Dahle, H., Lilje, P. B., Ridgway, S. E., 2002, MNRAS, 335, 1017

Worrall, D. M., Lawrence, C. R., Pearson, T. J., Readhead, A. C. S., 1994, ApJ, 420, L17

Worrall, D. M., Birkinshaw, M., Hardcastle, M. J., Lawrence, C. R., 2001, MNRAS, 326, 1127

Zirbel, E., L., 1997, ApJ, 476, 489

This figure "Appendix-F1.jpg" is available in "jpg" format from:

http://arxiv.org/ps/0709.3635v1

This figure "Appendix-F2.jpg" is available in "jpg" format from:

http://arxiv.org/ps/0709.3635v1

This figure "Appendix-F3.jpg" is available in "jpg" format from:

http://arxiv.org/ps/0709.3635v1

This figure "Appendix-F4.jpg" is available in "jpg" format from:

http://arxiv.org/ps/0709.3635v1

This figure "Appendix-F5.jpg" is available in "jpg" format from:

http://arxiv.org/ps/0709.3635v1